

HI content at cosmic noon – a millimeter-wavelength perspective

Hugo Messias^{1,2*}, Andrea Guerrero³, Neil Nagar³, Jack Regueiro⁴, Violette Impellizzeri⁵,
Gustavo Orellana⁶, Miguel Vioque^{1,7}

¹Joint ALMA Observatory, Alonso de Córdova 3107, Vitacura 763-0355, Santiago, Chile

²European Southern Observatory, Alonso de Córdova 3107, Vitacura, Casilla 19001, Santiago de Chile, Chile

³Departamento de Astronomía, Facultad de Ciencias Físicas y Matemáticas, Universidad de Concepción, Concepción, 4030000, Chile

⁴Princeton University Princeton, NJ 08544-1001 U.S.A.

⁵Leiden Observatory, Leiden University, PO Box 9513, 2300 RA, Leiden, The Netherlands

⁶Fundación Chilena de Astronomía, código postal 7500011, Santiago, Chile

⁷National Radio Astronomy Observatory, 520 Edgemont Road, Charlottesville, VA 22903, USA

Accepted XXX. Received YYY; in original form ZZZ

ABSTRACT

In order to understand galaxy growth evolution, it is critical to constrain the evolution of its building block: gas. Mostly comprised by Hydrogen in its neutral (HI) and molecular (H₂) phases, the latter is the one mostly directly associated to star-formation, while the neutral phase is considered the long-term gas reservoir. In this work, we make use of an empirical relation between dust emission at millimeter wavelengths and total gas mass in the inter-stellar medium (M_{HI} plus M_{H₂}) in order to retrieve the HI content in galaxies. We assemble an heterogeneous sample of 335 galaxies at $0.01 < z < 6.4$ detected in both mm-continuum and carbon monoxide (CO), with special focus on a blindly selected sample to retrieve HI cosmological content when the Universe was $\sim 2 - 6$ Gyr old ($1 < z < 3$). We find no significant evolution with redshift of the M_{HI}/M_{H₂} ratio, which is about 1 – 3 (depending on the relation used to estimate M_{HI}). This also shows that M_{H₂}-based gas depletion times are underestimated overall by a factor of 2 – 4. Compared to local Universe HI mass functions, we find that the number density of galaxies with M_{HI} $\gtrsim 10^{10.5} M_{\odot}$ significantly decreased since 8–12 Gyr ago. The specific sample used for this analysis is associated to 20–50% of the total cosmic HI content as estimated via Damped Lyman- α Absorbers. In IR luminous galaxies, HI mass content decreases between $z \sim 2.5$ and $z \sim 1.5$, while H₂ seems to increase. We also show source detection expectations for SKA surveys.

Key words: ISM: abundances – galaxies: ISM – submillimetre: ISM

1 INTRODUCTION

Over the last 25 years it has become increasingly clear that the star-formation (SF) history in the Universe peaked at about 10 Gyr ago (Lilly et al. 1996; Madau et al. 1998; Hopkins & Beacom 2006; Madau & Dickinson 2014). Nevertheless, it is only in the last 5 years, with the advent of spectral scan surveys conducted with Atacama Large (sub-)Millimeter Array (ALMA; Brown et al. 2004), Jansky Very Large Telescope (JVLA; Perley et al. 2011), and the Northern Extended Millimeter Array (NOEMA; Guilloteau et al. 1992), that the community has identified the driver of this effect in a statistically consistent manner. Namely, the cosmological content of molecular-Hydrogen (H₂) in the Inter-Stellar Medium (ISM) peaks at a similar epoch (Aravena et al. 2016; Decarli et al. 2019, 2020; Riechers et al. 2019; Lenkić et al. 2020).

After the fact, this may come as no surprise since: it is long known that star-formation rate surface density correlates well with total ISM gas – in either neutral or molecular phases — surface density (the so-called Schmidt-Kennicutt, SK, law; Schmidt 1959; Kennicutt 1998);

gas in regions with high SF efficiency is mostly in its molecular phase, while in less SF efficient regions gas is mostly in its neutral phase (HI) (Bigiel et al. 2008); and the SK law holds up to high redshifts (e.g., Bouché et al. 2007).

Nevertheless, both neutral and molecular Hydrogen components in galaxies are difficult to directly detect with increasing redshifts. The former, because of its low transition probability, while the latter due to the absence of a permanent dipole moment. Hence, indirect tracers are required if one aims to estimate their content in galaxies up to early cosmic times.

Historically, H₂ has been traced via Carbon Monoxide (CO) emission, with the ground based rotational transition (J:1-0) being the reference tracer. If a higher-J transition is available, population-wide line ratios (R_{JJ-10}) are usually adopted to estimate the ground transition emission (e.g., Carilli & Walter 2013). The H₂ mass can then be obtained from the CO-luminosity by considering a conversion factor (α_{CO10}) that remains a topic of discussion. Today, it is agreed that this factor is highly metallicity-dependent, and that in Solar-like metallicity environments, one can adopt the value found in the Milky-Way (see Dunne et al. 2022, and references therein). However, uncertainties in both R_{JJ-10} and α_{CO10} (among others) can easily build up

* E-mail: hugo.messias@eso.org

and result in significant uncertainties in the estimated molecular gas mass (M_{H_2}). With the advent of deep observations with ALMA and NOEMA, the community also now considers neutral Carbon (CI) as a molecular gas tracer, making use of its forbidden transitions $[\text{CI}]^3\text{P}_1 - ^3\text{P}_0$ and $^3\text{P}_2 - ^3\text{P}_1$. Despite being fainter than CO low-J transitions, its spectral line energy distributions (SLED) is simpler (only three levels), it is optically thin in most extra-galactic environments, and has fewer excitation mechanisms than CO (see [Dunne et al. 2022](#), and references therein). Nevertheless, this alternative also requires a conversion factor with an associated uncertainty and considerable telescope time.

On the other hand, neutral Hydrogen has only been directly detected up to $z \sim 0.2 - 0.4$ ([Lah et al. 2007](#); [Fernández et al. 2016](#)), and up to $z = 1.3$ with the aid of strong gravitational lensing ([Chakraborty & Roy 2023](#)). Otherwise, at high-redshifts, neutral gas has been mostly traced in absorption ([Rao et al. 2006](#); [Braun 2012](#); [Zafar et al. 2013](#)) and trace impact parameters in the 0.1–1 Mpc range, significantly larger than the typical visible galaxy size regardless of cosmic time or reference wavelength (i.e., galaxies at high-redshift are intrinsically smaller, ([Buitrago et al. 2008](#)), while the largest known galaxy is about 200 kpc in diameter ([Galaz et al. 2015](#))). Alternative approaches comprise methods making use of optical continuum emission (e.g., [Zhang et al. 2009](#); [Catinella et al. 2012](#); [Parkash et al. 2018](#); [Bera et al. 2022](#)), or combining the SK law with the relation between molecular gas fraction and the mid-plane pressure acting on a galaxy disc ([Popping et al. 2015](#), making use of [Bigiel et al. \(2008\)](#); [Blitz & Rosolowsky \(2006\)](#)).

In this work, we present a millimeter-wavelength-based method to estimate the neutral Hydrogen content in galaxies. In Section 2, we detail the methodological basis of our approach. In Section 3, we detail the sample assembled from the literature considered in our analysis. In Section 4, we report our results including the derived HI cosmological content at $1 \lesssim z \lesssim 3$, while in Section 5 we present our conclusions. The adopted cosmology refers to the results reported by [Planck Collaboration et al. \(2020, *Planck18* cosmology henceforth\)](#), namely $H_0 = 67.7 \text{ km s}^{-1} \text{ Mpc}^{-1}$ and $\Omega_M = 0.31$ (note that in some figures we also use the Hubble constant dimensionless equivalent $h_{P18} = 0.677$).

2 METHODOLOGY

2.1 Estimating ISM gas mass via dust continuum emission

The last decade has shown the potential of using the mm continuum emission of galaxies to retrieve their molecular-gas content up to very high redshifts ([Scoville et al. 2014, 2016, 2017](#); [Magnelli et al. 2020](#)). This is based on the fact that the Rayleigh-Jeans tail of the dust thermal emission in galaxies is mostly optically thin, thus being a tracer of the total dust mass ([Scoville et al. 2014](#); [Orellana et al. 2017](#), and references therein). The latter is related to the star-formation activity (both its production and heating; [Kennicutt & Evans 2012](#)), which is observed to be related to the molecular gas content ([Schmidt 1959](#); [Kennicutt 1998](#); [Bouché et al. 2007](#); [Bigiel et al. 2008](#)). This mm-continuum-based conversion factor (referenced to rest-frame $850 \mu\text{m}$, $\alpha_{850}^{\text{H}_2}$) has the great advantage that it requires significantly less telescope time while providing an estimated molecular-gas mass density evolution in the Universe in very good agreement with those based in line observations (Section 4.3).

The underlying assumption of $\alpha_{850}^{\text{H}_2}$ is that dust is well mixed with the molecular gas and mostly traces H_2 -dominated regions. However, this scenario is likely only applicable to the luminous-end of the KS-

law regime ([Bigiel et al. 2008](#)), and it has been shown that the M_{dust} (and as a result $850 \mu\text{m}$ luminosity, L_{850} , as a proxy) yields a tighter relation with the total gas mass ([Orellana et al. 2017](#); [Casasola et al. 2020](#)), thus including neutral gas (HI). In this work, total gas mass in the ISM refers to:

$$M_{\text{ISM}} = \alpha_{\text{heavy}} (M_{\text{HI}} + M_{\text{H}_2}) \quad (1)$$

where $\alpha_{\text{heavy}} = 1.36$ is the factor that corrects the gas mass estimate in order to account for chemical elements heavier than Hydrogen in the ISM ([Crowell 1996](#); [Carroll & Ostlie 2006](#)), and $M_{\text{H}_2} = \alpha_{\text{CO}}^{\text{H}_2} L'_{\text{CO}10}$. Unless otherwise stated, we adopt $\alpha_{\text{CO}}^{\text{H}_2} = 2.9$, which is the value reported by [Dunne et al. \(2022, \$\alpha_{\text{CO}}^{\text{H}_2} = 4.0\$ \)](#), but uncorrected for heavier element fraction.

In order to establish a relation between M_{ISM} and L_{850} we have adopted the sample used in [Orellana et al. \(2017, and references therein\)](#). Briefly, it comprises different types of galaxies found in the local-Universe ($z < 0.1$) for which reliable HI and CO detections are available in the literature.

In Figure 1 we specifically show how L_{850} relates with M_{H_2} (upper left panel), M_{HI} (upper right), and M_{ISM} (lower left). Two type of fits are shown in the panels, a log-log linear relation ($\log(L_{850}) = m \log(M_{\text{gas}}) + C$; red line and shaded region; referred to as LR method henceforth) and a 1-to-1 ratio ($\log(L_{850})/\log(M_{\text{gas}})$; blue line and shaded region; RT method henceforth). The lower-right panel also shows L_{850} versus M_{ISM} , but where $\alpha_{\text{CO}}^{\text{H}_2}$ was also left free in the fitting process (note that no priors were used to constrain the value). In each panel, we report the best fits (LR in red, RT in blue, the values in parenthesis shows the fit parameters uncertainties) together with the sample's standard deviation (STD) and median absolute deviation (MAD) in the x- and y-axis directions. For reference, we also show higher-redshift galaxies (yellow stars and square) for which there are also direct detections of HI, CO, and dust continuum ([Cybulski et al. 2016](#); [Cortese et al. 2017](#); [Fernández et al. 2016](#)), but were not used in the derived fits.

Quantitatively, based on each fit's resulting population STD and MAD values, it is clear that there is a fitting improvement from left to right, and top to bottom, with overall reductions in STD and MAD of 0.3 dex and 0.1 dex, respectively, for RT. The differences for the LR results are even larger. In the lower-right panel, the reported best-fit value for $\alpha_{\text{CO}}^{\text{H}_2}$ is 1.21 ± 0.10 . The improvement in the sample spread while using this value is small (< 0.1 dex), but we interpret this reduction in $\alpha_{\text{CO}}^{\text{H}_2}$ as a balancing of the neutral and molecular regions that L_{850} is tracing. In other words, there are galaxies or regions in galaxies where M_{H_2} and M_{HI} amount to similar quantities/masses. Considering them together would thus mean doubling the weight of such regions when deriving a fit (i.e., lower-left panel). As such, we interpret this value of $\alpha_{\text{CO}}^{\text{H}_2} = 1.21$ as the limit identifying the regions in galaxies in which L_{850} is tracing a dominant M_{H_2} component of the ISM gas. However, this interpretation needs a more careful analysis, and is deferred to future work. In this manuscript, since we wish to test the implications of using either RT or LT, we adopt $\alpha_{\text{CO}}^{\text{H}_2} = 1.21$ in the adopted RT and LT, but $\alpha_{\text{CO}}^{\text{H}_2} = 2.9$ when estimating total M_{H_2} . As a result, we adopt the following nomenclature throughout the manuscript:

$$M_{\text{ISM}} = \alpha_{\text{heavy}} (M_{\text{HI}} + 2.9 L'_{\text{CO}10}) \quad (2)$$

$$M_{\text{ISM}}^{\text{R}} = \alpha_{\text{heavy}} (M_{\text{HI}} + 1.21 L'_{\text{CO}10}) \quad (3)$$

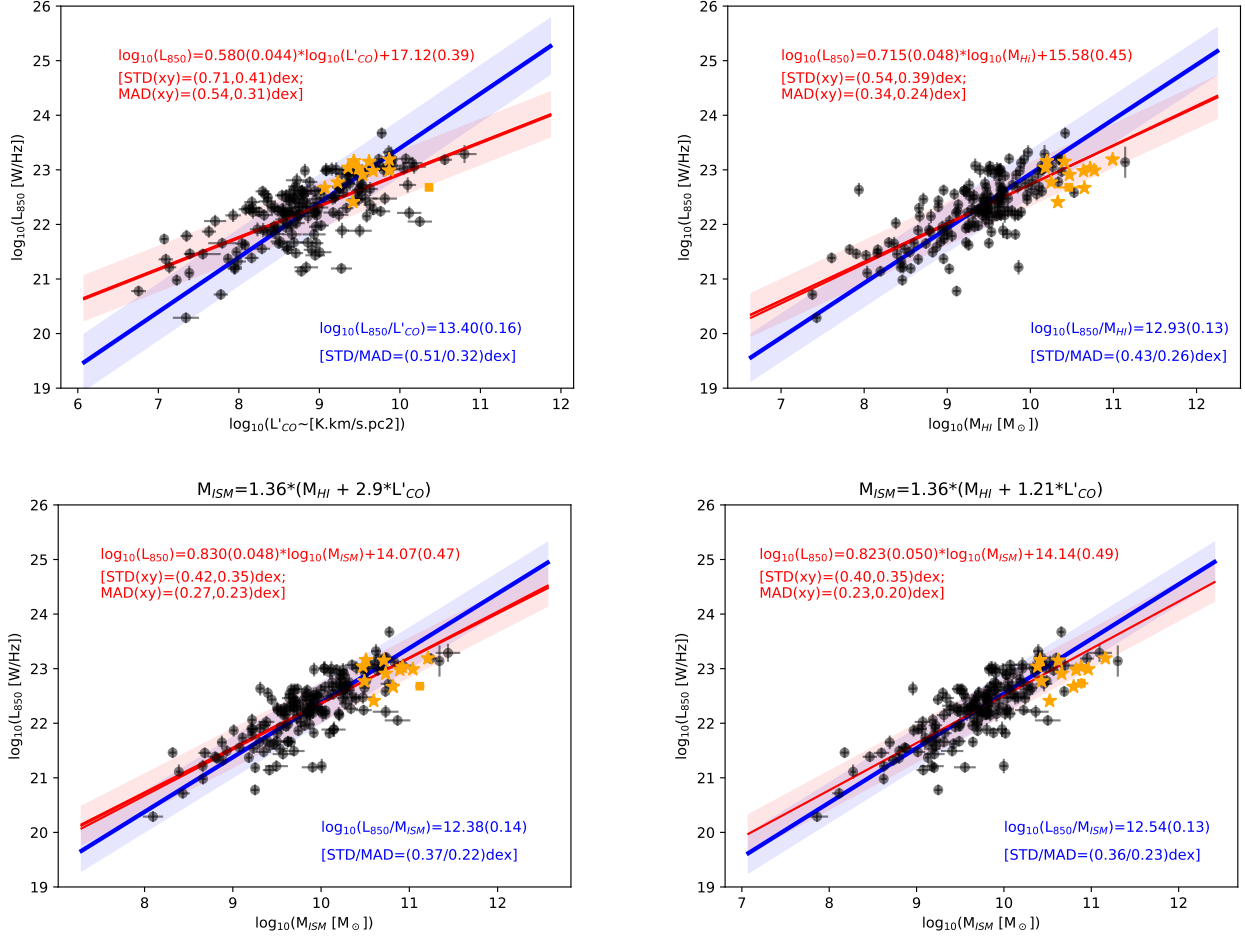


Figure 1. For the sample used in Orellana et al. (2017, black circles), we show how L_{850} relates to L'_{CO10} (as a tracer for M_{H_2} ; top left-hand side panel), M_{HI} (top right), M_{ISM} (bottom left; Equation 2), or M_{ISM}^R (bottom right; Equation 3). The blue line and region show the overall parameter ratio and the data standard deviation (STD) in the log-log space. The red line and region show the best linear fit to the data and its STD in the log-log space. The results are presented in each panel in the bottom right (ratio) and upper left (linear fit), together with the STD and the median absolute deviation (MAD) of the population in the x and y directions. The results from the bottom-right panel are the ones reported in Equations 4 and 5. An higher-redshift sample (Cybulski et al. 2016; Cortese et al. 2017; Fernández et al. 2016) is shown for reference (yellow data points), and intentionally not used in the analysis.

and the following relations:

$$RT \equiv \log\left(\frac{L_{850}[\text{W/Hz}]}{M_{ISM}^R[M_{\odot}]}\right) = 12.54(\pm 0.13) \quad (4)$$

$$LR \equiv \log(L_{850}[\text{W/Hz}]) = 0.823(\pm 0.050) \log(M_{ISM}^R[M_{\odot}]) + 14.14(\pm 0.49) \quad (5)$$

2.2 Rest-frame 850 μm continuum estimates

We have considered two different approaches in order to estimate the dust continuum flux density at rest-frame 850 μm (S_{850}^{RF}): (i) modified black body fit to FIR plus (sub-)mm photometry; (ii) power-law fit to (sub-)mm photometry ($S_{\nu} \propto \nu^{\beta}$). The former was pursued by making use of MBB EMCEE¹ (Foreman-Mackey et al. 2013; Conley 2016) to fit *Herschel* Space Observatory (*Herschel*; Pilbratt et al. 2010)

photometry together with 0.85–3 mm photometry when available. However, we soon found that this method overestimated S_{850}^{RF} when comparing the fit with and without (sub-)mm photometry. Sometimes, even considering the latter, the *Herschel* photometry weighted more to the fit, resulting in an overestimated S_{850}^{RF} . As a result, we do not consider those galaxies for which a (sub-)mm detection is not reported.

Approach (ii) was thus the only adopted approach to estimate S_{850}^{RF} . In Figure 2 we show the spectral-index distribution of the 54 sources for which more than one frequency photometry is reported. The median value of β is $3.35^{+0.58}_{-0.38}$ (MAD=0.27). This was the spectral-index adopted in cases where only one (sub-)mm photometry data point is available.

2.3 Converting high-J CO transitions to J:1-0

Although CO J:1-0 is the reference transition with which to estimate total M_{H_2} , it is a common practice to target a higher-J transition (e.g., $J_{\text{up}} = 2, 3, 4$), that, not only is brighter, less optically thick, but it is

¹ https://github.com/aconley/mbb_emcee

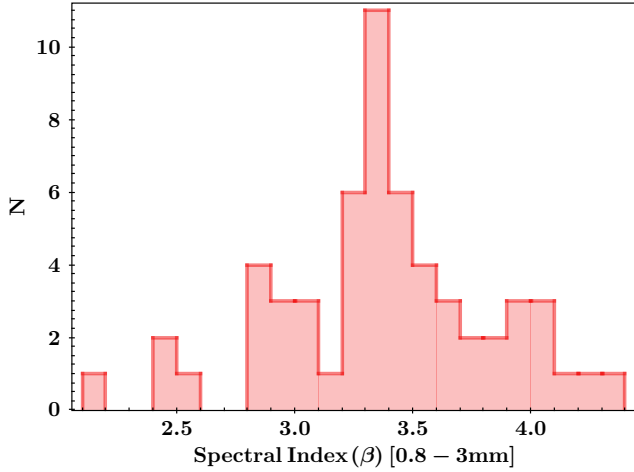


Figure 2. The distribution of the estimated spectral-index in the observed mm spectral range (0.8–3 mm) for 54 galaxies in our sample, for which there are more than one mm-photometry data points.

also found at frequencies where the dust continuum emission is also brighter. For that reason, one needs to consider the CO SLEDs to convert from the higher-J transition to the ground one. In this work, we adopt the line luminosity ratios reported for sub-millimeter galaxies in Table 2 in [Carilli & Walter \(2013\)](#) for the samples assembled from [Walter et al. \(2011\)](#), [Saintonge et al. \(2013\)](#), PHIBSS, [Birkin et al. \(2021\)](#), and any other galaxy in other samples at $z > 2$ (see Section 3 for sample details). Otherwise, we adopt the line luminosity ratios reported for galaxies at $1.0 < z < 1.6$ in [Boogaard et al. \(2020\)](#). We do this separation following the findings in [Boogaard et al. \(2020\)](#), acknowledging that selection effects tend to provide samples with more excited CO SLEDs at higher redshifts. We do note that the CO SLEDs reported by [Boogaard et al. \(2020\)](#) at $1.0 < z < 1.6$ are in line with those by [Daddi et al. \(2015\)](#), while the SMG CO SLEDs reported by [Carilli & Walter \(2013\)](#) are in line with those by [Bothwell et al. \(2013\)](#) and [Birkin et al. \(2021\)](#), and slightly lower than those by [Boogaard et al. \(2020\)](#) at $2.0 < z < 2.7$.

2.4 Corrections to a hotter CMB

Due to the adiabatic expansion of the Universe, the Cosmic Microwave Background (CMB) shows today a black-body spectral energy distribution characteristic of temperature of 2.73 K ([Fixsen 2009](#)), while, as we look back in time, the CMB shows a hotter temperature. This results in the molecular gas and dust becoming progressively in thermal equilibrium with the CMB, thus making it harder to detect emission against a brighter/hotter background emission ([da Cunha et al. 2013](#); [Zhang et al. 2016](#)). Here, we adopt the correction recipes proposed by [da Cunha et al. \(2013\)](#), namely, we make use of Equations 12 and 18 therein.

2.5 Estimating M_{HI}

In Equations 2 through 5, there are three main observables: S_{850} , $S_{\text{HI}}\Delta_{\nu}$, and $S_{\text{CO}}\Delta_{\nu}$. Thus, if one detects two of them, the third one can be inferred within the errors associated with both the photometric errors and the intrinsic population scatter shown in Figure 1. Nowadays, with the growing legacy of ALMA and NOEMA surveys, the most common scenario is when a (sub-)mm facility observes both

S_{850} and S_{CO} , sometimes in a single observation. As a result, in a statistical sense, one can attempt to derive the HI content in a galaxy population.

We thus combine Equation 2 with Equations 4 and 5 to determine M_{HI} :

$$M_{\text{HI}}^{\text{RT}} = \frac{10^{\log(L_{850}[\text{W/Hz}]) - 12.54}}{\alpha_{\text{heavy}}} - 1.21 L'_{\text{CO}10} \quad (6)$$

$$M_{\text{HI}}^{\text{LR}} = \frac{10^{(\log(L_{850}[\text{W/Hz}]) - 14.14)/0.823}}{\alpha_{\text{heavy}}} - 1.21 L'_{\text{CO}10} \quad (7)$$

We note that in cases where the derived M_{HI} is negative, we interpret such a result as a galaxy whose ISM gas component is mostly in its molecular phase.

2.6 Error budget

As one can see from the previous sub-sections, there are different steps involved up until when one retrieves the final HI mass estimate. In this section, we summarize the different uncertainties that are being considered in quadrature to retrieve the final error budget associated to the reported HI mass value:

- we have adopted the MAD values associated with the adopted relations (Section 2.1)
- we have considered population STD associated to the reported luminosity ratios between higher-J and J:1-0 transitions from [Boogaard et al. \(2020\)](#), while we have adopted a general error of 0.15 associated to the values reported by [Carilli & Walter \(2013\)](#), since no error is reported therein, but it is nevertheless in line with other works (e.g., [Boogaard et al. 2020](#); [Birkin et al. 2021](#))
- to the reported CO and continuum errors, we have added 10% of the flux in quadrature to account for absolute flux scaling systematics
- for those galaxies with only one photometry data point in the mm spectral range, we have considered the MAD associated to the adopted spectral index.

3 SAMPLE SELECTION

As stated in the previous section, in this manuscript, we make use of direct observations of mm-continuum and CO to infer the content of HI gas. As a result, we have assembled from the literature a sample of galaxies that have both a CO emission line detection and (sub-)mm continuum coverage. We mainly choose galaxies with a low- J_{up} CO transition (typically $J_{\text{up}} \leq 3$) in order to have a more reliable conversion to CO J:1-0.

As you will see ahead, specifically for the analysis of the cosmic HI mass content (Section 4.3), we focus only on two samples (Sections 3.1 and 3.2) which provide the simplest selection function.

3.1 ASPECS

We consider galaxies from the ALMA SPECTroscopic Survey in the Hubble Ultra-Deep Field (ASPECS) LP survey ([González-López et al. 2020](#); [Walter et al. 2016](#); [Aravena et al. 2016](#)) later followed up at lower frequencies by its VLA equivalent VLASPECS ([Riechers et al. 2020](#)). Both programs comprise blind surveys of CO covering an area of 4.6 arcmin². We focus on the CO $J_{\text{up}} = 1, 2, 3$ line measurements from [Boogaard et al. \(2020\)](#) for 18 galaxies. For those galaxies, we use the 1.2 mm continuum flux densities from [Aravena et al. \(2020\)](#)

and González-López et al. (2020), and the 3 mm flux densities from González-López et al. (2019). We also looked for other sub-mm observations and found a $870\ \mu\text{m}$ flux density measurement for the galaxy “1mm6” in the Chapin et al. (2011) catalog.

3.2 Birkin et al. (2021)

Birkin et al. (2021) presented ALMA and NOEMA observations of SMGs selected from the ALMA-SCUBA-2 Cosmic Evolution Survey (AS2COSMOS, total area of $1.6\ \text{deg}^2$; Simpson et al. (2020)), the ALMA-SCUBA-2 Ultra Deep Survey (AS2UDS, total area of $0.96\ \text{deg}^2$; Stach et al. (2019); Dudzevičiūtė et al. (2020)) and the ALMA-LABOCA ECDIFS Submillimetre Survey (ALESS, area of $30' \times 30'$; Hodge et al. (2013); Danielson et al. (2017)). The original catalog provides the $870\ \mu\text{m}$ and 3mm flux densities for 61 galaxies, along with CO emission lines, $J_{\text{up}} = 2-5$ for 50 of those galaxies.

For the HI mass density analysis in Section 4.3, we focus on the flux-selected galaxies within the “scan sample” in Birkin et al. (2021): 5 source with $S_{870} = 15 - 20\ \text{mJy}$ in AS2COSMOS and 13 sources with $S_{870} = 8 - 14\ \text{mJy}$ in AS2UDS. Note the complementary flux selection. In addition, we also considered the 13 optical/near-infrared faint galaxies within the “scan sample” and the 30 galaxies within the “*Spec - z* sample”.

3.3 COLDz

The CO Luminosity Density at High- z (COLDz; Pavesi et al. (2018)) survey is a blind survey of CO that covered $\sim 9\ \text{arcmin}^2$ of the COSMOS deep field and $\sim 51\ \text{arcmin}^2$ of the GOODS-North wide field. We found the sub-mm photometry in different surveys. For the galaxies COLDz.GN.31 and COLDz.COS.0 we found the $850\ \mu\text{m}$ flux density from the SCUBA-2 Cosmology Legacy Survey Geach et al. (2017); for the galaxies COLDz.GN.14 and COLDz.GN.16 we use the $850\ \mu\text{m}$ flux densities from the SUPER GOODS survey Cowie et al. (2017); for the galaxy COLDz.COS.11 we use the $1100\ \mu\text{m}$ flux density from the AzTEC millimetre survey of the COSMOS field Aretxaga et al. (2011); and finally, using both the Liu et al. (2018) and Jin et al. (2018) catalogs we adopted the $850\ \mu\text{m}$ photometry for the galaxies COLDz.GN.15, COLDz.GN.28, COLDz.COS.6, and both the $850\ \mu\text{m}$ and $1100\ \mu\text{m}$ photometry for the galaxies COLDz.GN.0 COLDz.GN.3, COLDz.COS.1, COLDz.COS.2, COLDz.COS.3. This resulted in 13 selected galaxies.

3.4 PHIBSS

The IRAM Plateau de Bure High- z Blue Sequence Survey (PHIBSS; Tacconi et al. 2013) observed the CO (3-2) line emission for 52 massive, main-sequence star-forming galaxies. These galaxies were chosen from UV/optical/IR surveys to study the molecular gas in galaxies near the cosmic star formation peak of normal galaxies, and were carefully selected to cover a complete M_* -SFR plane. They included two redshift bins, at $z \sim 1.1$ and ~ 2.2 . The first bin, $z = 1-1.5$ includes galaxies from the All-Wavelength Extended Groth Strip International Survey (AEGIS; Davis et al. 2007a), which includes imaging from X-ray to radio and optical spectroscopy. The higher redshift bin, $z = 2-2.5$, includes galaxies from Erb et al. (2006), Mancini et al. (2011), the *BzK* sample of Daddi et al. (2010), Magnelli et al. (2012) and the three lensed galaxies cB58 (Baker et al. 2004), “cosmic eye” (Coppin et al. 2007) and “eyelash” (Swinbank et al. 2010, also known as J2135-0102). We found sub-mm observations for some of these galaxies in the following catalogs/surveys. We include $850\ \mu\text{m}$ fluxes

from the main catalog of the SCUBA-2 Cosmology Legacy Survey (Geach et al. 2017) for the galaxy EGS13004291 and the fluxes for the catalog of the EGS deep field (Zavala et al. 2017) for the galaxies EGS13011155, EGS13011166, EGS13017707, EGS13018076. For the *BzK* galaxies we include the $1300\ \mu\text{m}$ fluxes from Magdis et al. (2012). From the Liu et al. (2018) catalog we include the $850\ \mu\text{m}$ flux for the BzK17999 galaxy and both the $850\ \mu\text{m}$ and $1100\ \mu\text{m}$ fluxes for the galaxies BzK12591 and PEPJ123633. For the lensed galaxy “eyelash”, we include the $850\ \mu\text{m}$ and $1200\ \mu\text{m}$ fluxes from Ivison et al. (2010); for the galaxy cB58 we include the $850\ \mu\text{m}$ flux from van der Werf et al. (2001); for “cosmic eye” we include the $1200\ \mu\text{m}$ flux from Saintonge et al. (2013); and for the galaxy Q1700-MD94 we include the $1200\ \mu\text{m}$ flux from Henríquez-Brocal et al. (2022). This results in 15 galaxies with sub-mm measurements from the PHIBSS sample.

3.5 PHIBSS2

The PHIBSS2 survey (Freundlich et al. 2019) is an extension of the PHIBSS sample, previously described. In this survey, the CO(2-1) line emission was detected for 60 normal star-forming galaxies at redshifts $z = 0.5 - 0.8$. These galaxies were drawn from the North field of the Great Observatories Origins Deep Survey (GOODS-N; Giavalisco et al. 2004), the Cosmic Evolution Survey (COSMOS; Scoville et al. 2007), and the AEGIS survey (Davis et al. 2007b). They were chosen because deep *HST*, good quality spectroscopy and UV/IR observations are available, while following similar selection criteria as in PHIBSS.

The sub-mm information was gathered from the following surveys/catalogs. For the galaxies XG55 and L14GN022 we used the $850\ \mu\text{m}$ fluxes from the SCUBA-2 Cosmology Legacy Survey (Geach et al. 2017); for the galaxies XC54, XF54 and L14EG008 we used the $850\ \mu\text{m}$ fluxes from the EGS deep field sample of the SCUBA-2 Cosmology Legacy Survey (Zavala et al. 2017); for the galaxy L14GN034 we used the $850\ \mu\text{m}$ flux from the SUPER GOODS survey Cowie et al. (2017). From the Liu et al. (2018) catalog we include the $850\ \mu\text{m}$ and $1100\ \mu\text{m}$ fluxes for the galaxy XA55. This results in 7 galaxies with sub-mm measurements.

3.6 Saintonge et al. (2013)

Saintonge et al. (2013) compiled a sample of 17 lensed galaxies to study dust and gas at the high redshifts of $z = 1.4 - 3.1$. This goal was achieved combining observations in the FIR with *Herschel* PACS/SPIRE, and of the CO (3-2) line emission, using the IRAM Plateau de Bure Interferometer (PdBI). Also, they include the 1.2mm continuum photometry from IRAM 30m, Max Planck Millimeter Bolometer array (MAMBO; Kreysa et al. 1998) and Submillimeter Array (SMA) observations. These galaxies are considered to be UV-bright lenses, that show similar SFRs and stellar masses to main-sequence galaxies at high redshift, thus, they are normal star-forming galaxies.

We selected 5 lensed galaxies, that are the detected CO (3-2) line. We discarded the sources cB58, Eye and Eyelash since they are part of the PHIBSS sample.

3.7 Seko et al. (2016)

The sample from Seko et al. (2016) is extracted from a larger one reported in Yabe et al. (2012) where 317 sources selected from optical and NIR surveys (SXDS/UDS; $0.67\ \text{deg}^2$) were followed-up

spectroscopically, with 71 being assigned a reliable redshift estimate. Of those, 20 were targeted by [Seko et al. \(2016\)](#), with 11 being detected in CO (5-4), of which 5 were detected in mm continuum.

3.8 VALES

The Valparaíso ALMA Line Emission Survey (VALES; [Villanueva et al. 2017](#)), used ALMA Band 3 to observe the CO(1-0) line emission in 67 galaxies in the redshift range $0.02 < z < 0.35$. This survey targeted galaxies from the Herschel Astrophysical Terahertz Large Area Survey (H-ATLAS; [Eales et al. 2010](#)), that covered a total area of $\sim 160 \text{ deg}^2$ of the sky ([Valiante et al. 2016](#)). These galaxies were selected because they are detected near the peak of the SED for a normal, local and dusty star-forming galaxy ([Villanueva et al. 2017](#)). The sample have reliable matches with the 6th Sloan Digital Sky Survey data release (SDSS; [Adelman-McCarthy et al. 2008](#)). The sample originates from two different selections involving criteria such as SDSS sizes or *Herschel* PACS spectroscopy.

Out of the 67 sources, 49 show a CO(1-0) line detection ($>5\sigma$). For 25 of these galaxies we found the 1 mm continuum using the ALMA archive, from the projects 2016.1.00994.S, 2017.1.01647.S, and 2017.1.00287.S. These observations are down to a depth of $\sim 0.02 \text{ mJy/beam}$, $\sim 0.003 \text{ mJy/beam}$ and $\sim 0.03 \text{ mJy/beam}$, respectively.

3.9 Walter et al. (2011)

[Walter et al. \(2011\)](#) compiled $850\mu\text{m}$, CO(3-2) and CI observations for different SMG galaxies. We selected 15 of their catalog galaxies for our sample, while the remainder were discarded due to the uncertainty on the magnification factor.

The sub-mm continuum flux information comes from: [Iverson et al. \(1998, SMM J02399-0136\)](#), [Benford et al. \(1999, BRI 1335-0417\)](#), [Iverson et al. \(2000, SMM J14011+0252\)](#), [Barvainis & Iverson \(2002, RX J0911+0551\)](#), [Barvainis & Iverson \(2002, F10214, Cloverleaf\)](#), [Isaak et al. \(2002, PSS J2322+1944\)](#), [Iverson et al. \(2002, SMM J163650+4057, SMM J163658+4105\)](#), [Chapman et al. \(2003, SMM J123549+6215\)](#), [Kneib et al. \(2004, SMM J16359+6612\)](#), [Robson et al. \(2004, SDSS J1148+5251\)](#), [Pope et al. \(2006, GN 20, GN 20.2\)](#)

3.10 Summary

Table 1 provides an overall perspective of each survey or sample considered here. It includes the number of sources, the range in redshift and, when appropriate, the survey areal size. The names in the first column are the aliases by which we will refer to the samples henceforth. Overall, we have assembled a total of 335 galaxies, selected in different wavelength regimes, from optical continuum or spectroscopy, to near-infrared and (sub-)millimeter. As mentioned already, the samples ASPECS and B21 are the samples providing the simplest selection function hence, these are the two samples used to compute the cosmic HI mass density content in Section 4.3.

The full sample is provided in a master table as supplementary material.

4 RESULTS

4.1 HI mass estimates

We derive non-zero and non-negative M_{HI} estimates for 149 and 145 galaxies while using the RT or LR methods (Section 2), respectively.

Table 1. Analysis Sample Summary — this table reports the different samples we have considered to retrieve HI mass content in this work. The first column reports the aliases used throughout the manuscript. The third to fifth columns report the redshift ranges each sample covers, their surveyed areas, and the number of galaxies in each one.

Sample	Reference	Redshift	Area	N
VALES	Villanueva et al. (2017)	0.01–0.35	160 deg ²	49
PHIBSS	Tacconi et al. (2013)	1.0–2.3	0.41 deg ²	23
PHIBSS2	Freundlich et al. (2019)	0.50–0.78	—	60
S13	Saintonge et al. (2013)	1.4–2.7	—	5
W11	Walter et al. (2011)	2.2–6.4	—	14
ASPECS	Walter et al. (2016)	0.5–2.7	4.6 arcmin ²	20
COLDz	Pavesi et al. (2018)	2.0–5.3	60 arcmin ²	58
S16	Seko et al. (2016)	1.3–1.6	0.77 deg ²	11
B21	Birkin et al. (2021)	1.2–4.8	2.81 deg ²	50
Total				335

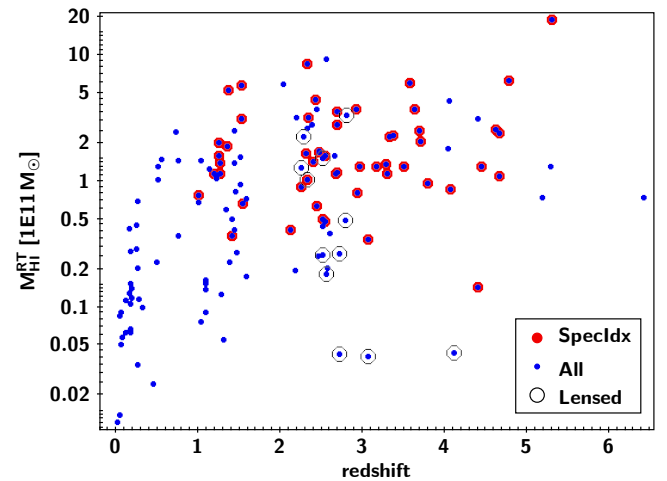


Figure 3. The $M_{\text{HI}}^{\text{RT}}$ distribution with redshift for 149 with non-zero and non-negative M_{HI} estimates adopting the RT method. The values do not consider the contribution of heavier elements. Galaxies that have more than one photometry data points in the mm spectral range (labelled SpecIdx) are highlighted by red dots. Galaxies that are known lensed galaxies are highlighted by empty black circles. For the latter, the plotted values are corrected for gravitational magnification.

In Figure 3, we show the $M_{\text{HI}}^{\text{RT}}$ distribution with redshift. We highlight those galaxies that have more than one photometry data points in the mm spectral range (red dots), and those which are known lensed galaxies (empty black circles; magnification-corrected values are displayed). There are no clear deviations between these groups, except for a few lensed galaxies understandably showing lower masses. If one instead plots $M_{\text{HI}}^{\text{LR}}$ the data points will shift to higher M_{HI} values by a median factor of 4.3 (with a spread of 0.18 dex or a factor of 1.5) as shown in Figure 4 (see also Section 4.2). This is expected given the flatter slope of the LR estimate, that implies a higher M_{HI} component for the same L_{850} and L'_{CO} values with respect to RT.

4.2 ISM gas mass fractions

We now compare the M_{HI} and the M_{H_2} content in our sample. This comparison is shown in Figure 5 for both RT and LR. For reference in the top panel, we mark the equal-content level as a dotted-line,

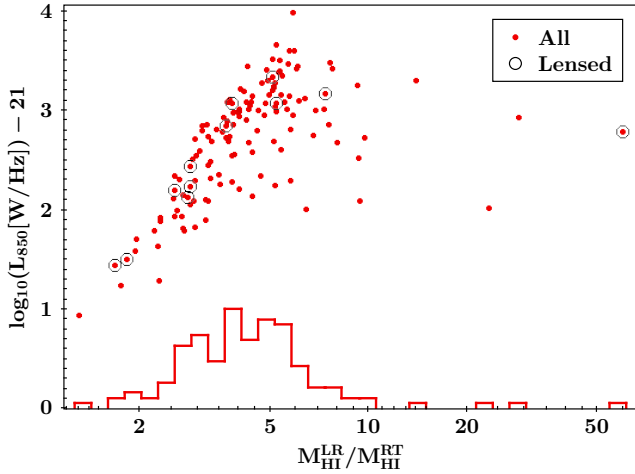


Figure 4. The ratio between the M_{HI} estimates derived with LR and RT methods versus L_{850} . A total of 137 galaxies, for which both methods predict non-zero/negative values, are used in this plot. For reference, the lensed galaxies are highlighted with black circles. The inset histogram is a normalized one to show the distribution of the data set. The distribution shows that LR predicts a median factor of ~ 4 higher M_{HI} content than the RT method. The y-axis was normalized to 10^{21} for display better visual comparison between the scatter plot and the histogram.

and the median values for RT (dashed blue) and LR (dashed red) methods. The color coding reflects L_{850} . For reference, $L_{850} = 10^{23}$ and 10^{24} W/Hz are approximately the LIRG and ULIRG thresholds (based on Equation E.5 in Orellana et al. 2017). The middle and bottom panels in Figure 5 show the dependency of the $M_{\text{HI}}/M_{\text{H}_2}$ ratio with redshift or L_{850} , respectively, for the RT and LR methods (black and red color, respectively). The sample was divided into quantiles, within which the median value is estimated (thick lines). The boxes show where 68% of the population within each quantile falls. These ranges were estimated based on a Bootstrapping analysis, where, for each gas ratio estimate and associated error, we randomly draw 100 new values assuming a log-normal distribution. From these we then retrieve the 16th and 84th percentiles which delimit the boxes. Overall, there is no significant evidence for evolution of the $M_{\text{HI}}/M_{\text{H}_2}$ ratio with redshift or L_{850} , except if one adopts the LR method which may imply higher ratios with increasing L_{850} (red trend in bottom panel). This is not unexpected, since it is at the highest luminosities that the two relations deviate more from each other (Figure 1).

We do note that Chowdhury et al. (2022) reports $M_{\text{HI}}/M_{\text{H}_2}$ ratios of $2-5^2$ for a sample of galaxies with $M^* = 1.03 \pm 0.24 \times 10^{10} M_{\odot}$ at $0.74 < z < 1.45$. Although this is in line with the overall value of 2.9 ($-0.42, +0.36$ dex) using LR method, versus 0.8 ($-0.56, +0.33$ dex) using RT, the galaxy population is different. For those galaxies in our analysis sample at $0.74 < z < 1.45$ that have reported stellar mass estimates in the literature, 95% have $\sim M^* > 10^{10.2} M_{\odot}$. Also, the gas mass fractions are sample-selection dependent. Despite the ratio values just mentioned for the analysis sample assembled in this work, the ASPECS and B21 samples used in Section 4.3 show lower values with different deviations in each redshift bin. Namely, the $M_{\text{HI}}/M_{\text{H}_2}$ ratio is 0.9 at $z \sim 1.5$ and 0.5 at $z \sim 2.5$ when using the RT method,

² One detail worth noting is that Chowdhury et al. (2022) estimate the molecular gas content based on a relation dependent on stellar mass and specific star formation rate.

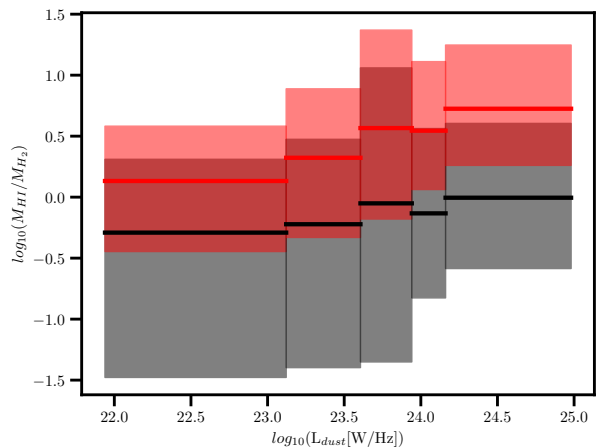
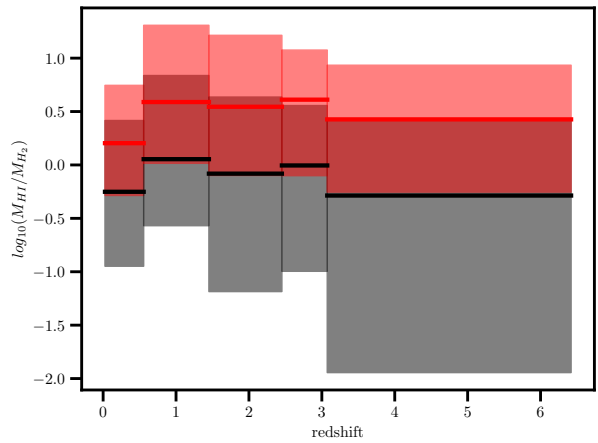
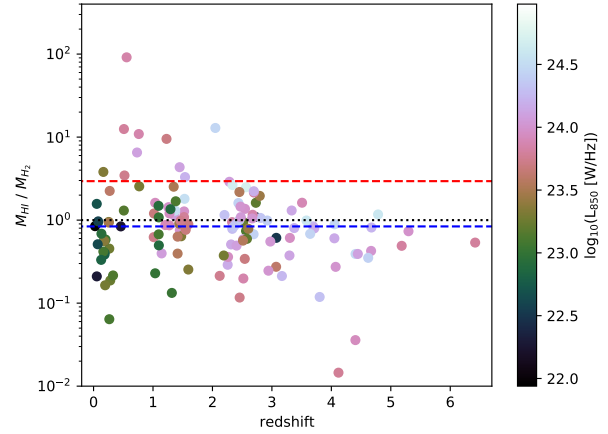


Figure 5. Distribution of $M_{\text{HI}}/M_{\text{H}_2}$ ratio with redshift and L_{850} . *Top panel:* The data points show the results adopting RT. The color coding reflects L_{850} . For reference, we mark the equal-content level as a dotted-line, and the median values for RT (dashed blue) and LR (dashed red) methods. *Middle panel:* The dependency of $M_{\text{HI}}/M_{\text{H}_2}$ ratio on redshift separating the sample into quantiles. The thick lines show the median value in each quantile (red and black lines for LR and RT methods, respectively). Each box shows where 68% of the population falls (16th and 84th percentiles) based on a Bootstrapping analysis (see details in the text). *Bottom panel:* Same as in the middle panel, but with respect to L_{850} .

and 2.4 and 2.8 when using LR. This goes in line with the fact that these samples are truly dust- and CO-selected (as opposed to other samples that are, e.g., selected in the optical-NIR), hence more likely to yield a larger molecular gas fraction (see next Section 4.3).

4.3 HI mass functions and overall gas density

In this section, we use only the samples from ASPECS and B21 since these are the samples with the simplest selection function, because it only depends on the continuum and CO selections. In the B21 sample, we only consider the sub-sample referred to as “scan sample” (point i-a) therein. We decided not to use the COLDz sample, since the catalogue includes lower fidelity line detections, but the fidelity values are not reported. ASPECS and B21 spectral scans cover similar redshift ranges of interest to this work: $1.01 < z < 1.81$ and $2.01 < z < 3.20$. The samples are quite complementary, where ASPECS covers better the $M_{\text{H}_2} < 6.5 \times 10^{10} M_{\odot}$ regime, and B21 otherwise. We used this M_{H_2} value as threshold above/below which we considered the B21/ASPECS samples. We do this to prevent double counting sources with M_{H_2} values around that threshold while using the V_{max} approach (see next paragraph), especially those above the adopted threshold present in ASPECS since cosmic variance may become critical. Nevertheless, Appendix B does show the implications of not adopting this mitigation approach.

In order to determine the volumetric representativeness of each galaxy we adopt the V_{max} method. In order to determine the minimum and maximum redshifts (z_{min} and z_{max}), we consider both the continuum and CO fluxes. The minimum redshift is basically given by the limits of the spectral scans adopted in each survey. To estimate z_{max} , we not only consider the significance of the flux in the detection band and the estimated or adopted spectral-index, but also the significance of the CO detection.

In Figure 6, we show the derived gas mass functions (MFs) for both M_{H_2} (top left-hand panel) and M_{HI} (top right) and compare them with estimates from the literature. All the M_{H_2} measurements from the literature have been converted to the α_{CO} value adopted in this work, and, once more, we do not correct for heavier elements. The agreement with the literature (Decarli et al. 2019; Riechers et al. 2019; Decarli et al. 2020; Lenkić et al. 2020) is noticeable.

The top right-hand panel shows the results for M_{HI} using the RT method. The local-Universe MFs from Zwaan et al. (2005); Martin et al. (2010); Jones et al. (2018) are also displayed for reference (all limited to $M_{\text{HI}} < 10^{11} M_{\odot}$). Since the uncertainties in the derived M_{HI} estimate do spread over more than one bin (we adopted a standard bin width of 0.5 dex), we actually distribute the measurement probability per bin assuming a log-normal error distribution since otherwise the massive-end would be underestimated (see Bera et al. 2022, we note that we have also adopted this approach while retrieving the H_2 MFs). We do note that the peaks of distribution may not relate to the intrinsic shape of the functions, but may instead show the mass limit below which each sample is complete at each redshift range. Conservatively, we have thus made the data points more translucent below those thresholds. The thresholds adopted in the H_2 MFs are those from the literature, while those in the H_1 MFs are where one sees the trend inflex (+0.5 and +1 dex higher for RT and LR methods, respectively, with respect to H_2 MFs). Nevertheless, the result seems to point that the main difference in HI content with respect to the local Universe happens in galaxies with $M_{\text{HI}} \gtrsim 10^{10.5} M_{\odot}$.

The next step is thus to retrieve the cosmological mass density evolution of both dominant ISM gas constituents. In Figure 7 we show measurements from the literature and compare them with our results (left-hand side panel using the RT method, right panel using the LR

one). In order to allow for a Cosmology-independent comparison with the literature, what is depicted in the figure is the cosmological mass density:

$$\Omega_{\text{gas}} = \frac{\rho_{\text{gas}}}{\rho_{\text{crit}}} \quad (8)$$

where

$$\rho_{\text{crit}} = \frac{3 H_0^2}{8\pi G} \quad (9)$$

is today’s Universe critical density. Blue color refers to HI gas, while black/gray refers to H_2 . None of the data points have been corrected for heavier elements.

The assembly of literature measurements for H_2 mass density are also of two types, either from CO detections (Decarli et al. 2020, grey-line limited boxes) or inferred from mm-continuum (Scoville et al. 2017, continuous grey-line limited region). All data have been converted so that the same α_{CO} is adopted. Our results for H_2 mass density (gray-filled boxes) are quite in agreement with those from the literature (Appendix B shows the results if no M_{H_2} -cut is applied between ASPECS and B21 samples). The fact that Scoville et al. (2017) shows a higher cosmological content may be the result of sample incompleteness toward lower M_{H_2} affecting the CO-selected sample. The Scoville et al. (2017) approach was to estimate M_{H_2} with a dependence on redshift, stellar mass, and specific SFR. This allowed the team to account for a more representative population at cosmic noon (see discussions in Sections 3.2 and 10 in Scoville et al. 2017).

The thin blue crosses at the top of Figure 7 are the literature measurements for HI mass density (Zwaan et al. 2005; Lah et al. 2007; Rao et al. 2006; Martin et al. 2010; Braun 2012; Zafar et al. 2013). We note that the measurements above redshift 0.3 are obtained via damped Lyman- α absorption systems, while the local Universe ($z \leq 0.24$) measurements are direct detections of the 21 cm line. Our results are shown as thick-line blue error-bars. Within the uncertainties, there is no significant evolution from $z \sim 2.5$ and $z \sim 1.5$. This happens irrespective of the HI-estimate method one adopts, the difference being that RT shows that CO/dust-selected samples recover $23 \pm 12\%$ and $17 \pm 11\%$ of the overall HI mass density at $z \sim 1.5$ and $z \sim 2.5$, respectively, while the LR method points to $61 \pm 27\%$ and $53 \pm 33\%$.

What both methods clearly show is that LIRG-type galaxies have a significant decrease in HI gas content during the same time range (by factors of 0.5 ± 0.4 and 0.4 ± 0.3 for RT and LR methods, respectively; data points shown as blue triangles). Doing the same exercise for the H_2 gas content for the same sub-sample (data points shown as black triangles), we find instead an increase of a factor of 1.4 ± 0.8 , even though with less significance. This trend may explain the drop in SFR density seen for this kind of galaxies since $z \sim 1$ (Le Floch et al. 2005; Goto et al. 2011; Magnelli et al. 2011).

4.4 Sources of contamination

Actively accreting super-massive black holes (or Active Galactic Nuclei, AGN) may appear bright at radio wavelengths, to the point that their mm-emission is still dominated by synchrotron emission from the jet (e.g., Messias et al. 2021). If that is the case, then the individual L_{850} estimates will become overestimated, and those of M_{HI} will too as a result (Equations 6 and 7). This may result in a large impact in the cosmic mass density based on a small sample like the one used here.

To test this hypothesis we cross-matched the ASPECS and Birkin

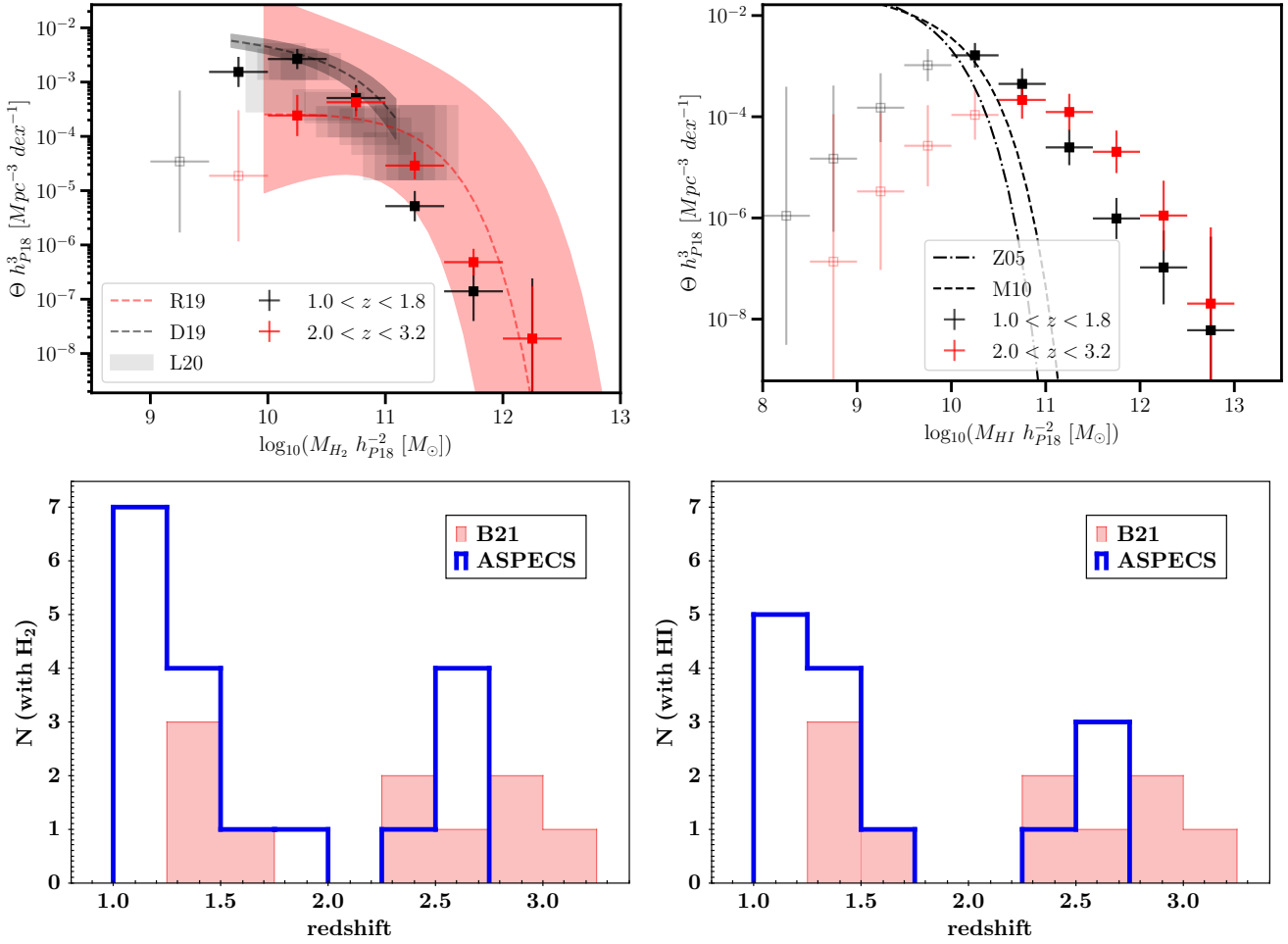


Figure 6. The mass functions (MFs; top row) for M_{H_2} (left-hand side panel) and M_{HI} (right panel; results for the RT method) obtained with the ASPECS and B21 samples. Black and red data points refer, respectively, to the following redshift bins: $1.01 < z < 1.81$, $2.01 < z < 3.20$. The literature H_2 MFs come from Decarli et al. (2019), dashed black line and gray shaded region; $\langle z \rangle \approx 1.43$, Lenkić et al. (2020, gray boxes; $z \sim 1 - 2$), and Riechers et al. (2019, red dashed line and shaded region; $2 < z < 3$). The literature M_{HI} MFs are those reported in the local Universe by Zwaan et al. (2005, dashed-dotted line), Martin et al. (2010, dashed line; Jones et al. (2018) results match this one). Translucent data points are indicative of the mass thresholds below which the MFs are believed to be incomplete. The bottom row reports the redshift distributions for ASPECS (blue histogram) and B21 (red shaded region) samples used in this analysis. The left-hand side panel shows the distribution of sources with M_{H_2} estimates, and the right panel shows those with positive M_{HI} estimates with the RT method.

et al. (2021) samples with the radio catalogues reported by Simpson et al. (2006, UDS; 1.4 GHz), Kellermann et al. (2008, GOODS-South; 1.4 GHz), Smolčić et al. (2017, COSMOS; 3 GHz). We only find matches with the Birkin et al. (2021) sample of sub-millimeter galaxies (SMGs): a total of 13 sources. One with a counterpart separation of 2 arcsec, and the remainder at < 1 arcsec. Only 3 of the matched sources are used in Section 4.3. Following the approach by Messias et al. (2021), we predict the contribution of the synchrotron emission at rest-frame $850 \mu\text{m}$ adopting the radio flux estimates and a spectral index of $\alpha = -0.7$ (where $S_{\nu} \propto \nu^{\alpha}$). We find that 12 sources show an observed-to-predicted flux ratio of $\sim 4 - 24$ (median of 13), while one (ALESS071.1) shows a ratio of 0.1, which is evidence for its mm emission to be synchrotron-dominated. Curiously enough, the M_{HI} estimate for ALESS071.1 is actually negative (i.e., the ISM gas is mostly in its molecular phase) using either RT or LR methods. Finally, only three sources are also used in Section 4.3 (AS2COS0014.1, AS2UDS627.0, AS2UDS029.0), and for these we find ratios of 16, 9.8, 21 (respectively). Given the order-of-scale difference, we consider these sources not to have a significant

synchrotron contribution to their luminosities at rest-frame $850 \mu\text{m}$, which also implies that our inferred HI cosmic mass densities are not contaminated (i.e., biased high) due to AGN contamination.

5 CONCLUSIONS

5.1 The evolution of the HI gas mass density

As mentioned in the previous section, the cosmological HI gas mass density shows no significant evolution for this CO/dust-selected sample at $1 \lesssim z \lesssim 3$. However, we have reasons to believe that this sample is significantly incomplete in the $z \sim 2.5$ redshift range especially when we compare our H_2 content results with those from Scoville et al. (2017) based on a purely dust-selected sample. If the missing population contributes significantly to the overall HI mass density, then the evolution may be a decreasing one with time from $z \sim 2.5$ to ~ 1.5 . This is already apparent if one limits the analysis to the brightest galaxies: $L_{850} > 10^{23} \text{ W/Hz}$ (for which our sample is expected to be somewhat complete, Figure 8). This LIRG-like sub-sample shows

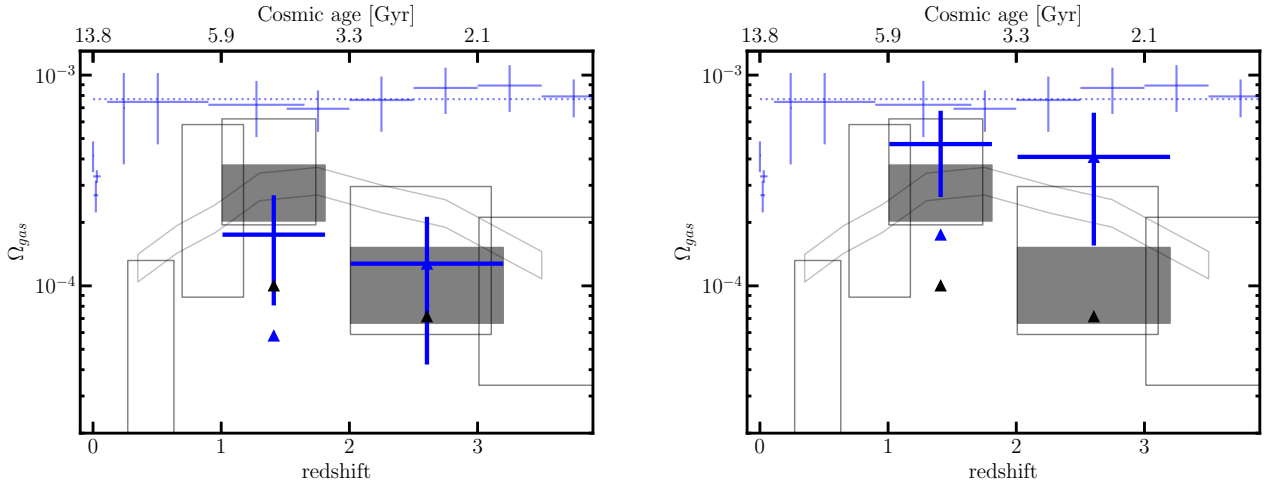


Figure 7. The ISM gas mass cosmological density evolution of its neutral and molecular phases. Left-hand side panel shows the results adopting the RT method, while the right-hand side panel shows those adopting the LR method. Blue error-bars refer to HI gas mass density measurements from the literature, while grey-line limited regions to H₂ gas mass literature estimates (see text for details). The thick line error-bars and grey filled boxes show our results. The blue and black triangles show the HI and H₂ gas mass densities, respectively, for sources with $L_{850} > 10^{23}$ W/Hz (LIRG-type galaxies).

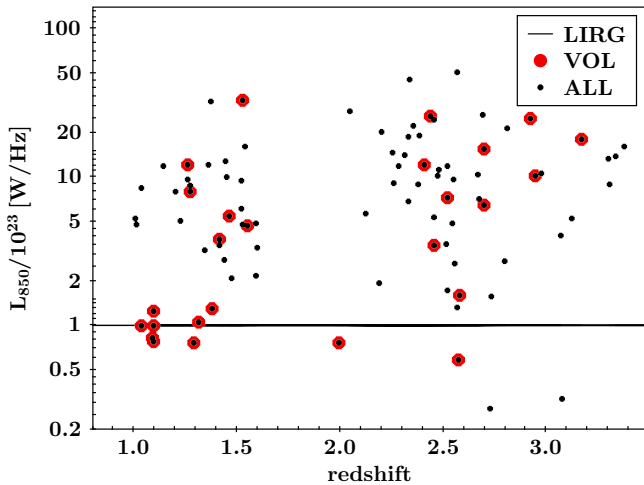


Figure 8. The distribution of L_{850} with redshift for the sample considered in this work, zoomed-in to the redshift range of interest in Section 4.3. The sample used for the cosmic gas density content ("VOL") is highlighted with red dots. For reference, the horizontal line shows the LIRG-like luminosity threshold.

a decrease in HI content of a factor of 2 during this time range, while an increase of a factor of 1.4 in H₂ gas content. This drop in neutral gas inflow may be the reason for the drop in SFR density seen for this kind of galaxies starting ~ 3 Gyr later, i.e., since $z \sim 1$ (Le Flocc'h et al. 2005; Goto et al. 2011; Magnelli et al. 2011). The current uncertainties in our analysis are large enough to prevent us from determining how much HI is being converted into H₂ between these two redshift bins for this LIRG-like population (currently the errorbars are consistent with all missing HI being converted into H₂).

5.2 ISM gas depletion times

In Figure 5, we show that, overall, there is a 1-to-1 (RT) or 3-to-1 (LR) HI-to-H₂ content ratio, with no clear signs of evolution with

redshift, except at the highest luminosities (Figure 6). This is thus a hint that the usual depletion times quoted in the literature taking into account only the H₂ content are underestimated by a factor of 2 to 4. However, this is very much sample-selection dependent, since the CO/dust-selected sample used for the cosmological gas content evolution analysis shows median HI-to-H₂ content ratios of 0.9 and 0.5 at $z \sim 1.5$ and ~ 2.5 , respectively, when using the RT method. Nevertheless, this still shows that a significant ISM gas content (at least a third) is not being considered for the estimate of gas depletion times.

For a quantitative example, we make use of the 12 SMGs reported in Section 4.4 not to have significant AGN contamination in the radio ($1.2 < z < 4.8$). For these we estimated the SFR adopting the calibration based on the 1.4 GHz continuum emission reported in Murphy et al. (2011) (that assumes the initial mass function from Kroupa 2001):

$$\text{SFR}_{1.4\text{GHz}} [\text{M}_{\odot} \text{yr}^{-1}] = 6.35 \times 10^{-22} L_{1.4\text{GHz}} [\text{WHz}^{-1}] \quad (10)$$

This retrieves a median SFR of $930 \text{ M}_{\odot}/\text{yr}$ (with a minimum–maximum of $\sim 500\text{--}2000 \text{ M}_{\odot}/\text{yr}$). We find that the median depletion time ($\tau_{\text{SFR}} = M_{\text{H}_2}/\text{SFR}$) considering only $\alpha_{\text{heavy}} M_{\text{H}_2}$ is $\sim 410 \text{ Myr}$ (with a minimum–maximum of $\sim 260\text{--}730 \text{ Myr}$). If we instead consider the total ISM gas mass (Equation 1) adopting the RT method, the median τ_{SFR} is now $\sim 880 \text{ Myr}$ ($\sim 350\text{--}1600 \text{ Myr}$), while adopting the LR method, the values become $\tau_{\text{SFR}} \sim 2700 \text{ Myr}$ ($\sim 710\text{--}5600 \text{ Myr}$). These depletion time values assuming the total ISM gas mass are in line with the predictions from the cosmological hydrodynamic galaxy formation simulation of SMGs reported by Narayanan et al. (2015).

Moreover, in light of the latest findings on Giant Molecular Clouds (GMCs) lifetimes and SF efficiencies (Chevance et al. 2023, and references therein) we would like to raise awareness on the usage of the $M_{\text{H}_2}/\text{SFR}$ ratio to estimate τ_{SFR} of a system. GMCs in the Milky-Way and other local galaxies are found to have lifetimes of $\tau_{\text{GMC}} = 10 - 30 \text{ Myr}$ (Feldmann & Gnedin 2011; Murray 2011; Jeffreson & Kruijssen 2018), their SF efficiency is found to be $\epsilon_{\text{SF}} = 2 - 10\%$ (Kruijssen et al. 2019; Chevance et al. 2020), while the cloud mass distribution can be described with a power-law of the

form $dN/dM \propto M^c$, where $-2.5 < c < -1.5$ (Murphy et al. 2011; Mok et al. 2020; Chevance et al. 2023).

We have ran a simple exercise to test how the GMC constraints impose a deviation from the simple M_{H_2} /SFR ratio assumption. We first start randomly drawing GMC masses from the cloud mass distribution assuming $c = -2$ (Mok et al. 2020, and references therein) within a mass range of 10^4 to $10^8 M_\odot$ (i.e., GMC scales; Murray 2011; Chevance et al. 2023). In every iteration, we impose that the total cloud mass does not exceed the total mass in M_{H_2} , and that the SFR at τ_{GMC} lifetime scales (i.e., SFR per iteration: $\text{SFR}_{\text{GMC}}^{\text{iter}} = M_{\text{H}_2}^{\text{iter}} \times \epsilon_{\text{SF}} / \tau_{\text{GMC}}$) does not exceed the total SFR. The latter condition is to account for the fact that the commonly used long-wavelength or SED-based SFRs are values integrated over 100 Myr (Table 1 in Kennicutt & Evans 2012), while GMC lifetimes are 3 to 10 times shorter. So, that condition translates to: $\text{SFR}_{\text{GMC}}^{\text{iter}} \leq \text{SFR}_{\text{tot}} * \tau_{\text{GMC}} [\text{Myr}] / 100$. After each iteration, we sum the adopted τ_{GMC} to the cumulative of τ_{SFR} , and the used up molecular mass ($M_{\text{H}_2}^{\text{iter}} \times \epsilon_{\text{SF}}$) is reduced from the $M_{\text{H}_2}^{\text{tot}}$. The iterations continue until the leftover $M_{\text{H}_2}^{\text{tot}}$ is $\leq 10^6 M_\odot$ (a scale at the level of the mass on a single GMC). This exercise shows that the M_{H_2} /SFR ratio gives similar gas depletion timescales as adopting $\tau_{\text{GMC}} = 10$ or 20 Myr and ϵ_{SF} of 5 or 10%, respectively. If one instead adopts the middle expected values for τ_{GMC} (20 Myr) and ϵ_{SF} (5%; also the typical value in the Milky Way, Williams & McKee 1997), then one finds that τ_{SFR} doubles with respect to the simple M_{H_2} /SFR ratio. This assumption is roughly the same as when one randomly draws in each iteration values of τ_{GMC} and ϵ_{SF} assuming a flat probability distribution. As a result, we suggest the following statistical correction to τ_{SFR} when estimated considering only M_{H_2} :

$$\tau_{\text{SFR}} = C_1 * C_2 * \frac{M_{\text{H}_2}}{\text{SFR}} \quad (11)$$

Where C_1 corrects for the existence of a HI reservoir, and C_2 corrects for the τ_{GMC} and ϵ_{SF} constraints. A value of $C_1 = 1$ is equivalent to a molecular gas dominated system, but the population wide results from this work point to $C_1 \geq 2$ (Section 4.2). Note that these values of C_1 assume no extra time delay related to gas transitioning from a neutral to a molecular phase, nor molecular gas dissociation (see section 3.2 in Chevance et al. 2023). As for C_2 , if we adopt average values for τ_{GMC} and ϵ_{SF} , then $C_2 = 2$, but once again we note that no dependence was assumed for these two parameters on cloud mass or size (see, for instance, Mok et al. 2020). For that reason, we provide as supplementary material the code used to conduct this exercise in case the reader wishes to build upon the assumptions described above.

5.3 Implications to SKA

As a simple exercise, we make predictions of the HI flux for the sample we have gathered in this work. In order to do so, we use:

$$S_{\text{HI}} = \frac{M_{\text{HI}} * (1+z)}{236 * D^2 * \Delta v} \quad (12)$$

where Δv is adopted to be 300 km/s and a Gaussian-like profile is assumed (even though a double peaked profile is more characteristic of typical galaxies). The line peak fluxes for both RT and LR methods are shown in Figure 9. For reference, we also show the expected fluxes from different M_{HI} values with redshift. The expected SKA 1h on-source integration 3σ sensitivity limit is shown (Braun et al. 2017, 2019). This figure shows that SKA will detect some of the galaxies assembled in this work at least up to $z \sim 0.5$ within 1 h. Above that redshift, it becomes more uncertain, with the both methods implying

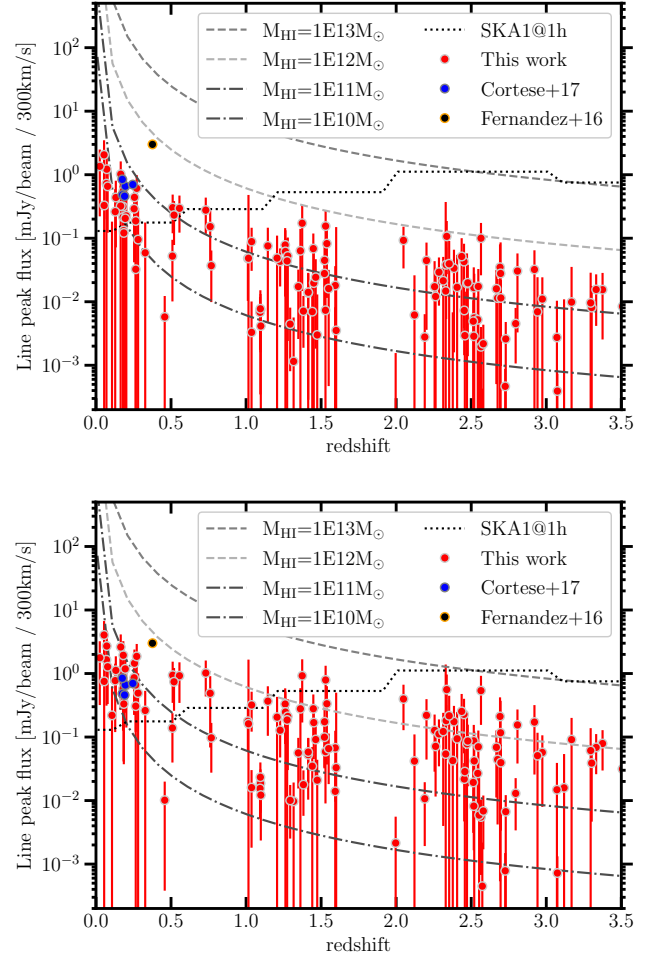


Figure 9. Predicted HI fluxes adopting the RT (top) and LR (bottom) methods for the sample considered in this work (red dots and errorbars). For reference, literature cases with direct HI detections at $0.2 < z < 0.5$ are also shown (Cortese et al. 2017; Fernández et al. 2016), as well as expected fluxes for different M_{HI} contents with redshift ($\log(M_{\text{HI}}) = 10\text{--}13$). The 1h on-source integration 3σ sensitivity of SKA1 is shown as a dotted line.

that, at $z > 2$, SKA needs to spend at least ~ 100 h to directly detect the bulk of these CO- and continuum-selected galaxies. Based on the obtained HI mass functions (Section 4.3, Figures 6 and A1), Table 2 resumes the expected number of galaxies directly detected by SKA, depending on time on source (ToS = 1, 100 h) and method used to estimate M_{HI} (RT and LR). We separate the estimates in redshift bins given the sensitivity differences in SKA Band 1 at 480–650 MHz ($1.2 < z < 2.0$) and 350–480 MHz ($2.0 < z < 3.1$)³. Note that 100 h limits the direct detections to $M_{\text{HI}} \geq 10^{11} M_\odot$, where we expect the analysis to be complete. Nevertheless, this sample is still limited by its CO- and continuum-detection nature, hence these numbers should be considered lower limits. Having this, large programs or stacking analysis will be required to characterize the star-forming population at these cosmic times.

³ SKA is expected to cover each of these frequency ranges in a single observation, so the ToS value is per frequency range reported.

ToS h	Scenario $\Delta\nu$ [MHz]	redshift	Method		Mass Limit [$\log(M_{\odot})$]
			RT	LR	
1	480–650	1.2–2.0	$0.5^{+4.2}_{-0.38}$	$3.0^{+5.4}_{-1.4}$	12
	350–480	2.0–3.1	$0^{+1.2}$	$0.55^{+4.6}_{-0.42}$	13
100	480–650	1.2–2.0	120^{+140}_{-62}	960^{+1200}_{-520}	11
	350–480	2.0–3.1	$7.9^{+31}_{-6.2}$	160^{+140}_{-72}	12

Table 2. Expected number of galaxies per deg^2 at $1 < z < 3$ directly detected by SKA based on the obtained HI mass functions (Section 4.3, Figures 6 and A1). We show the numbers for different times on source (ToS) and adopting either RT or LR to estimate M_{HI} . Note that 100 h ToS limits the direct detections to $M_{\text{HI}} \geq 10^{11} M_{\odot}$.

ACKNOWLEDGEMENTS

HM and JR acknowledge the ALMA-Princeton International Internship program, while HM and AG acknowledge the NRAO REU Chile Program and the SSDF ESO program, all of which allowed for the basis of this work to develop up to this stage.

HM would like to thank George Privon for the useful conversation about the recent results on GMRT HI surveys.

The team would like to thank the teams cited in Table 1 for making their results and data public, without which this work would have not been possible.

This research made use of IPYTHON (Perez & Granger 2007), NUMPY (van der Walt et al. 2011), MATPLOTLIB (Hunter 2007), SCIPY (Virtanen et al. 2020), ASTROPY (a community-developed core PYTHON package for Astronomy, Astropy Collaboration et al. 2013), and TOPCAT (Taylor 2005).

DATA AVAILABILITY

The inclusion of a Data Availability Statement is a requirement for articles published in MNRAS. Data Availability Statements provide a standardised format for readers to understand the availability of data underlying the research results described in the article. The statement may refer to original data generated in the course of the study or to third-party data analysed in the article. The statement should describe and provide means of access, where possible, by linking to the data or providing the required accession numbers for the relevant databases or DOIs.

REFERENCES

Adelman-McCarthy J. K., et al., 2008, *ApJS*, **175**, 297
 Aravena M., et al., 2016, *ApJ*, **833**, 68
 Aravena M., et al., 2020, *ApJ*, **901**, 79
 Aretxaga I., et al., 2011, *MNRAS*, **415**, 3831
 Astropy Collaboration et al., 2013, *A&A*, **558**, A33
 Baker A. J., Tacconi L. J., Genzel R., Lehnert M. D., Lutz D., 2004, *ApJ*, **604**, 125
 Barvainis R., Ivison R., 2002, *ApJ*, **571**, 712
 Benford D. J., Cox P., Omont A., Phillips T. G., McMahon R. G., 1999, *ApJ*, **518**, L65
 Bera A., Kanekar N., Chengalur J. N., Bagla J. S., 2022, *ApJ*, **940**, L10
 Bigiel F., Leroy A., Walter F., Brinks E., de Blok W. J. G., Madore B., Thornley M. D., 2008, *AJ*, **136**, 2846
 Birkin J. E., et al., 2021, *MNRAS*, **501**, 3926
 Blitz L., Rosolowsky E., 2006, *ApJ*, **650**, 933
 Boogaard L. A., et al., 2020, *ApJ*, **902**, 109

Bothwell M. S., et al., 2013, *MNRAS*, **429**, 3047
 Bouché N., et al., 2007, *ApJ*, **671**, 303
 Braun R., 2012, *ApJ*, **749**, 87
 Braun R., Bonaldi A., Bourke T., Keane E., Wagg J., 2017, *SKA memo*, pp [SKA–TEL–SKO–0000818](#)
 Braun R., Bonaldi A., Bourke T., Keane E., Wagg J., 2019, *arXiv e-prints*, p. [arXiv:1912.12699](#)
 Brown R. L., Wild W., Cunningham C., 2004, *Advances in Space Research*, **34**, 555
 Buitrago F., Trujillo I., Conselice C. J., Bouwens R. J., Dickinson M., Yan H., 2008, *ApJ*, **687**, L61
 Carilli C. L., Walter F., 2013, *ARA&A*, **51**, 105
 Carroll B. W., Ostlie D. A., 2006, *An introduction to modern astrophysics and cosmology*
 Casasola V., et al., 2020, *A&A*, **633**, A100
 Catinella B., et al., 2012, *A&A*, **544**, A65
 Chakraborty A., Roy N., 2023, *MNRAS*, **519**, 4074
 Chapin E. L., et al., 2011, *MNRAS*, **411**, 505
 Chapman S. C., et al., 2003, *ApJ*, **585**, 57
 Chevance M., et al., 2020, *Space Sci. Rev.*, **216**, 50
 Chevance M., Krumholz M. R., McLeod A. F., Ostriker E. C., Rosolowsky E. W., Sternberg A., 2023, in Inutsuka S., Aikawa Y., Muto T., Tomida K., Tamura M., eds, *Astronomical Society of the Pacific Conference Series Vol. 534, Protostars and Planets VII*. p. 1 ([arXiv:2203.09570](#)), [doi:10.48550/arXiv.2203.09570](#)
 Chowdhury A., Kanekar N., Chengalur J. N., 2022, *ApJ*, **935**, L5
 Conley A., 2016, *mbb_emcee: Modified Blackbody MCMC*, *Astrophysics Source Code Library*, record ascl:1602.020 (ascl:1602.020)
 Coppin K. E. K., et al., 2007, *ApJ*, **665**, 936
 Cortese L., Catinella B., Janowiecki S., 2017, *ApJ*, **848**, L7
 Cowie L. L., Barger A. J., Hsu L. Y., Chen C.-C., Owen F. N., Wang W. H., 2017, *ApJ*, **837**, 139
 Crosswell K., 1996, *The alchemy of the heavens*.
 Cybulski R., et al., 2016, *MNRAS*, **459**, 3287
 Daddi E., et al., 2010, *ApJ*, **713**, 686
 Daddi E., et al., 2015, *A&A*, **577**, A46
 Danielson A. L. R., et al., 2017, *ApJ*, **840**, 78
 Davis M., et al., 2007a, *ApJ*, **660**, L1
 Davis M., et al., 2007b, *ApJ*, **660**, L1
 Decarli R., et al., 2019, *ApJ*, **882**, 138
 Decarli R., et al., 2020, *ApJ*, **902**, 110
 Dudzevičiūtė U., et al., 2020, *MNRAS*, **494**, 3828
 Dunne L., Maddox S. J., Papadopoulos P. P., Ivison R. J., Gomez H. L., 2022, *MNRAS*, **517**, 962
 Eales S., et al., 2010, *PASP*, **122**, 499
 Erb D. K., Steidel C. C., Shapley A. E., Pettini M., Reddy N. A., Adelberger K. L., 2006, *ApJ*, **647**, 128
 Feldmann R., Gnedin N. Y., 2011, *ApJ*, **727**, L12
 Fernández X., et al., 2016, *ApJ*, **824**, L1
 Fixsen D. J., 2009, *ApJ*, **707**, 916
 Foreman-Mackey D., Hogg D. W., Lang D., Goodman J., 2013, *PASP*, **125**, 306
 Freundlich J., et al., 2019, *A&A*, **622**, A105
 Galaz G., Milovic C., Suc V., Busta L., Lizana G., Infante L., Royo S., 2015, *ApJ*, **815**, L29
 Geach J. E., et al., 2017, *MNRAS*, **465**, 1789
 Gialalisco M., et al., 2004, *ApJ*, **600**, L93
 González-López J., et al., 2019, *ApJ*, **882**, 139
 González-López J., et al., 2020, *ApJ*, **897**, 91
 Goto T., et al., 2011, *MNRAS*, **410**, 573
 Guilloteau S., et al., 1992, *A&A*, **262**, 624
 Henríquez-Brocal K., et al., 2022, *A&A*, **657**, L15
 Hodge J. A., et al., 2013, *ApJ*, **768**, 91
 Hopkins A. M., Beacom J. F., 2006, *ApJ*, **651**, 142
 Hunter J. D., 2007, *Computing in Science & Engineering*, **9**, 90
 Isaak K. G., Priddey R. S., McMahon R. G., Omont A., Peroux C., Sharp R. G., Withington S., 2002, *MNRAS*, **329**, 149

Ivion R. J., Smail I., Le Borgne J. F., Blain A. W., Kneib J. P., Bezecourt J., Kerr T. H., Davies J. K., 1998, *MNRAS*, 298, 583

Ivion R. J., Dunlop J. S., Smail I., Dey A., Liu M. C., Graham J. R., 2000, *ApJ*, 542, 27

Ivion R. J., et al., 2002, *MNRAS*, 337, 1

Ivion R. J., et al., 2010, *A&A*, 518, L35

Jefferson S. M. R., Kruijssen J. M. D., 2018, *MNRAS*, 476, 3688

Jin S., et al., 2018, *ApJ*, 864, 56

Jones M. G., Haynes M. P., Giovanelli R., Moorman C., 2018, *MNRAS*, 477, 2

Kellermann K. I., Fomalont E. B., Mainieri V., Padovani P., Rosati P., Shaver P., Tozzi P., Miller N., 2008, *ApJS*, 179, 71

Kennicutt Robert C. J., 1998, *ApJ*, 498, 541

Kennicutt R. C., Evans N. J., 2012, *ARA&A*, 50, 531

Kneib J.-P., van der Werf P. P., Kraiberg Knudsen K., Smail I., Blain A., Frayer D., Barnard V., Ivion R., 2004, *MNRAS*, 349, 1211

Kreysa E., et al., 1998, in Phillips T. G., ed., Society of Photo-Optical Instrumentation Engineers (SPIE) Conference Series Vol. 3357, Advanced Technology MMW, Radio, and Terahertz Telescopes. pp 319–325, doi:10.1117/12.317367

Kroupa P., 2001, *MNRAS*, 322, 231

Kruijssen J. M. D., et al., 2019, *Nature*, 569, 519

Lah P., et al., 2007, *MNRAS*, 376, 1357

Le Floch E., et al., 2005, *ApJ*, 632, 169

Lenkić L., et al., 2020, *AJ*, 159, 190

Lilly S. J., Le Fevre O., Hammer F., Crampton D., 1996, *ApJ*, 460, L1

Liu D., et al., 2018, *ApJ*, 853, 172

Madau P., Dickinson M., 2014, *ARA&A*, 52, 415

Madau P., Pozzetti L., Dickinson M., 1998, *ApJ*, 498, 106

Magdis G. E., et al., 2012, *ApJ*, 760, 6

Magnelli B., Elbaz D., Chary R. R., Dickinson M., Le Borgne D., Frayer D. T., Willmer C. N. A., 2011, *A&A*, 528, A35

Magnelli B., et al., 2012, *A&A*, 548, A22

Magnelli B., et al., 2020, *ApJ*, 892, 66

Mancini C., et al., 2011, *ApJ*, 743, 86

Martin A. M., Papastergis E., Giovanelli R., Haynes M. P., Springob C. M., Stierwalt S., 2010, *ApJ*, 723, 1359

Messias H. G., et al., 2021, *MNRAS*, 508, 5259

Mok A., Chandar R., Fall S. M., 2020, *ApJ*, 893, 135

Murphy E. J., et al., 2011, *ApJ*, 737, 67

Murray N., 2011, *ApJ*, 729, 133

Narayanan D., et al., 2015, *Nature*, 525, 496

Orellana G., et al., 2017, *A&A*, 602, A68

Parkash V., Brown M. J. I., Jarrett T. H., Bonne N. J., 2018, *ApJ*, 864, 40

Pavesi R., et al., 2018, *ApJ*, 864, 49

Perez F., Granger B. E., 2007, *Computing in Science & Engineering*, 9, 21

Perley R. A., Chandler C. J., Butler B. J., Wrobel J. M., 2011, *ApJ*, 739, L1

Pilbratt G. L., et al., 2010, *A&A*, 518, L1

Planck Collaboration et al., 2020, *A&A*, 641, A6

Pope A., et al., 2006, *MNRAS*, 370, 1185

Popping G., et al., 2015, *MNRAS*, 454, 2258

Rao S. M., Turnshek D. A., Nestor D. B., 2006, *ApJ*, 636, 610

Riechers D. A., et al., 2019, *ApJ*, 872, 7

Riechers D. A., et al., 2020, *ApJ*, 896, L21

Robson I., Priddey R. S., Isaak K. G., McMahon R. G., 2004, *MNRAS*, 351, L29

Saintonge A., et al., 2013, *ApJ*, 778, 2

Schmidt M., 1959, *ApJ*, 129, 243

Scoville N., et al., 2007, *ApJS*, 172, 1

Scoville N., et al., 2014, *ApJ*, 783, 84

Scoville N., et al., 2016, *ApJ*, 820, 83

Scoville N., et al., 2017, *ApJ*, 837, 150

Seko A., Ohta K., Yabe K., Hatsukade B., Akiyama M., Iwamuro F., Tamura N., Dalton G., 2016, *ApJ*, 819, 82

Simpson C., et al., 2006, *MNRAS*, 372, 741

Simpson J. M., et al., 2020, *MNRAS*, 495, 3409

Smolčić V., et al., 2017, *A&A*, 602, A1

Stach S. M., et al., 2019, *MNRAS*, 487, 4648

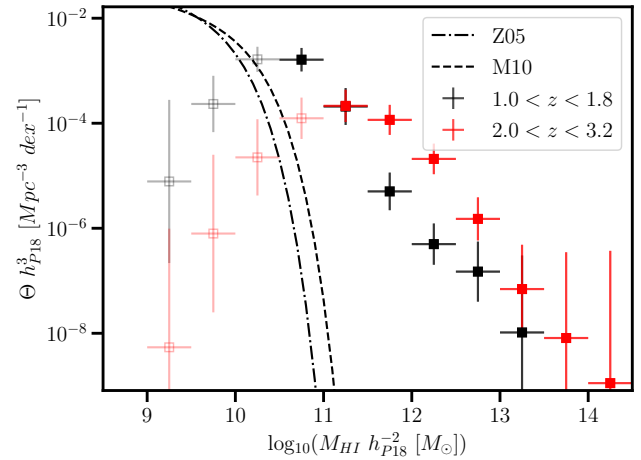


Figure A1. The same as in the top right-hand side panel of Figure 6, but adopting the LR method.

Swinbank A. M., et al., 2010, *Nature*, 464, 733

Tacconi L. J., et al., 2013, *ApJ*, 768, 74

Taylor M. B., 2005, in Shopbell P., Britton M., Ebert R., eds, Astronomical Society of the Pacific Conference Series Vol. 347, Astronomical Data Analysis Software and Systems XIV. p. 29

Valiante E., et al., 2016, *MNRAS*, 462, 3146

Villanueva V., et al., 2017, *MNRAS*, 470, 3775

Virtanen P., et al., 2020, *Nature Methods*, 17, 261

Walter F., Weiß A., Downes D., Decarli R., Henkel C., 2011, *ApJ*, 730, 18

Walter F., et al., 2016, *ApJ*, 833, 67

Williams J. P., McKee C. F., 1997, *ApJ*, 476, 166

Yabe K., et al., 2012, *PASJ*, 64, 60

Zafar T., Péroux C., Popping A., Milliard B., Deharveng J. M., Frank S., 2013, *A&A*, 556, A141

Zavala J. A., et al., 2017, *MNRAS*, 464, 3369

Zhang W., Li C., Kauffmann G., Zou H., Catinella B., Shen S., Guo Q., Chang R., 2009, *MNRAS*, 397, 1243

Zhang Z.-Y., Papadopoulos P. P., Ivion R. J., Galametz M., Smith M. W. L., Xilouris E. M., 2016, *Royal Society Open Science*, 3, 160025

Zwaan M. A., Meyer M. J., Staveley-Smith L., Webster R. L., 2005, *MNRAS*, 359, L30

da Cunha E., et al., 2013, *ApJ*, 766, 13

van der Walt S., Colbert S. C., Varoquaux G., 2011, *Computing in Science & Engineering*, 13, 22

van der Werf P. P., Knudsen K. K., Labbé I., Franx M., 2001, in Lowenthal J. D., Hughes D. H., eds, Deep Millimeter Surveys: Implications for Galaxy Formation and Evolution. pp 103–106 (arXiv:astro-ph/0010459), doi:10.1142/9789812811738_0017

APPENDIX A: RESULTS WITH LR METHOD

In this section, we complete Figure 6 by showing the HI mass functions using the LR method in Figure A1.

APPENDIX B: RESULTS WITHOUT THE M_{H_2} -CUT

As mentioned in Section 4.3, we have adopted a cut in M_{H_2} between samples ASPECS and B21 so to guarantee complementary between the two. Nevertheless, here we present the results (Figures B1 and B2) when such a cut is not applied. The main differences to highlight are: the expected increase in cosmic gas content in both gas

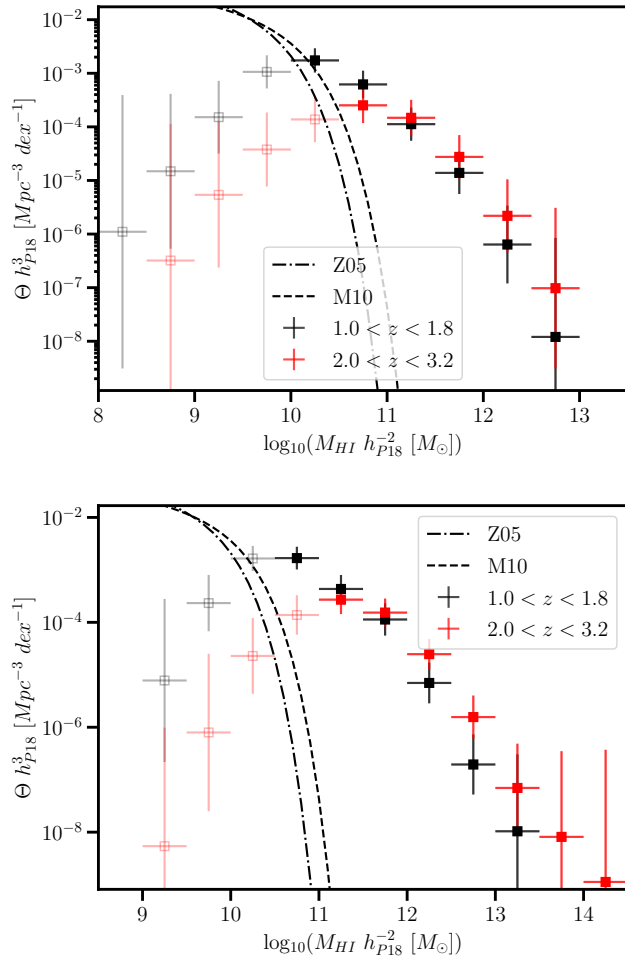


Figure B1. The same as in the top right-hand side panel of Figure 6, but not applying the cut in M_{H_2} . Top panel considers the RT method, while the bottom one the LR method.

phases (most noticeably in M_{H_2}) and redshift bins; the LR method implies that, within the errors bars, the samples extracted from ASPECS and B21 already recover the M_{HI} content estimated from DLA systems analysis; the sample at $z \sim 2.5$ still shows evidence for incompleteness with respect to the S17 approach; the M_{HI} content from the LIRG-like population is constant, but the M_{H_2} content still increases.

This paper has been typeset from a $\text{\TeX}/\text{\LaTeX}$ file prepared by the author.

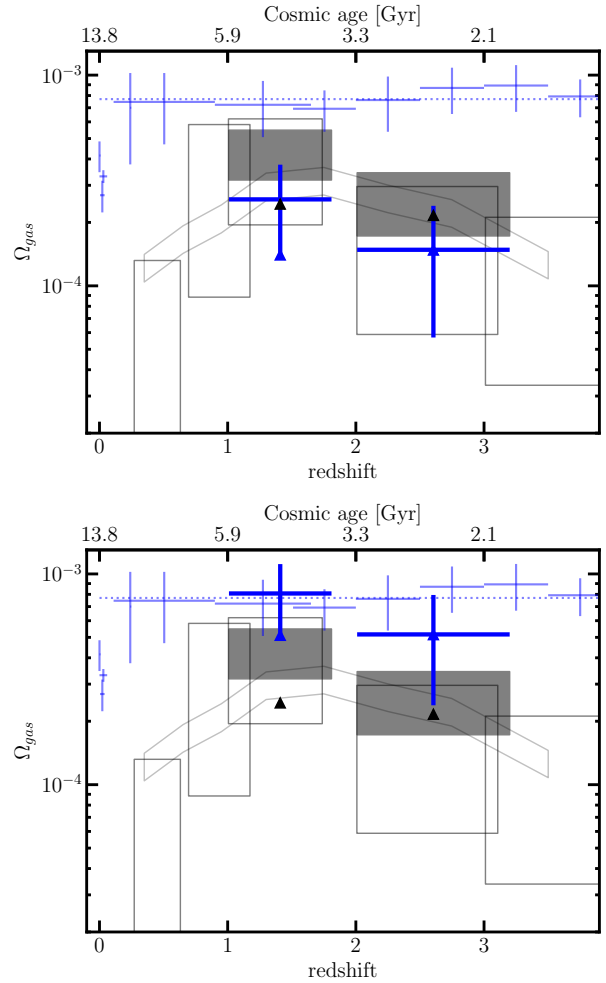


Figure B2. The same as in Figure 7, but not applying the cut in M_{H_2} . Top panel considers the RT method, while the bottom one the LR method.